Journal of Materials Chemistry A

ROYAL SOCIETY OF CHEMISTRY

PAPER

View Article Online
View Journal | View Issue

Check for updates

Cite this: *J. Mater. Chem. A*, 2025, **13**, 9211

Perovskite oxides as a new family of tunable CO_2 sorbents†

Seyedamin Razavi, Vahid Rahmanian, Runxia Cai, Mahe Rukh, Saad A. Khan and Fanxing Li *

Received 29th November 2024
Accepted 26th February 2025

DOI: 10.1039/d4ta08481k

rsc.li/materials-a

CO_2 adsorption using solid sorbents represents an attractive option for carbon capture due to its potential for low energy consumption, ease of operation, and higher stability. This study introduces perovskite oxides as a new family of highly tunable solid sorbents, with remarkable structural and compositional flexibility to tailor their sorption thermodynamics and kinetics. Using $Sr_xLa_{1-x}FeO_3$ (x = 0, 0.2, 0.5, and 0.7) as a model system, we demonstrated that varying the A-site composition of the perovskite oxide leads to substantial change in the CO_2 adsorption and desorption behavior, allowing a tunable CO_2 release within a temperature range of 75 to 500+ °C. A strong correlation between the oxide surface area and sorption capacity was also established. Despite the low surface area inherent to perovskite oxides, we managed to enhance their surface area from 3–5 $m^2\ g^{-1}$ (prepared by a salt assisted reactive grinding method) to ~30 $m^2\ g^{-1}$ using electrospun nanofibers. $Sr_{0.2}La_{0.8}FeO_3$ prepared *via* electrospinning exhibited a relatively moderate desorption temperature (onset: 120 °C and peak: 240 °C) and a CO_2 sorption capacity of 0.68 wt%. Analysis of the adsorption isotherms indicates that CO_2 is chemisorbed on the $Sr_{0.2}La_{0.8}FeO_3$ sorbent at low CO_2 partial pressures (0–1 kPa). Physisorption becomes dominant at higher pressures. Transmission electron microscopy (TEM) characterization revealed that perovskite synthesis *via* the electrospinning method results in the formation of perovskite nanorods. X-ray photoelectron spectroscopy indicates significantly higher surface La concentration when compared to oxides prepared with conventional methods. It was further determined that a higher surface La concentration is highly desirable for reversible CO_2 sorption. This study demonstrates tunable perovskite oxides as a new family of CO_2 sorbent materials and the potential to further enhance their surface area towards practical applications in CO_2 capture and utilization.

1 Introduction

The primary driving force behind global climate change is the accumulation of carbon dioxide (CO_2) in the Earth's atmosphere. As per the Intergovernmental Panel on Climate Change (IPCC), if no significant intervention occurs, CO_2 emissions are anticipated to surge from the current rate of 36 Gt per year to a range between 48 and 55 Gt per year by 2050.[1] This increase in emissions is primarily attributed to a substantial increase in energy demand, which is projected to grow by 40% to 150% during the same period. Recovering from an unavoidable excess of atmospheric CO_2 concentrations demands proactive removal of CO_2.[2] Achieving this necessitates the deployment of technologies capable of effectively capturing and permanently eliminating CO_2 from the atmosphere.[3]

The primary technologies investigated for CO_2 capture include cryogenic distillation, membrane separation, liquid absorption, and solid adsorption.[4] Cryogenic distillation imposes significant limitations on CO_2 capture due to its high energy requirements and the need for an initial step to eliminate compounds such as H_2O, SO_x, and NO_x.[4] Membrane separation is efficient when dealing with high concentrations of CO_2. However, its effectiveness and selectivity decline when CO_2 is not a substantial component in the stream. Solvent absorption is a well-established technology for CO_2 capture.[4] However, it comes with a significant energy cost for solvent regeneration and is susceptible to corrosion issues and volatility concerns.[5–7] In this context, adsorption using solid sorbents emerges as an appealing alternative which offers potential to reduce the energy expenditure and to mitigate corrosion concerns. Its efficiency, coupled with the simplicity of operation, makes it a promising option for carbon capture from diluted CO_2 streams.[4]

Capturing CO_2 from ambient air, also known as Direct Air Capture (DAC), can complement point-source capture by addressing emissions from dispersed sources that are not reachable through point-source capture methods.[8–10] Additionally, DAC can compensate for any residual emissions that escape during point-source capture.[8–10] The majority of air

Chemical and Biomolecular Engineering Department, College of Engineering, North Carolina State University, 911 Partners Way, Raleigh, NC, USA. E-mail: fli5@ncsu.edu

† Electronic supplementary information (ESI) available. See DOI: https://doi.org/10.1039/d4ta08481k

capture methods employ solid sorbents. Each of the sorbents under investigation utilizes one of two potential adsorption mechanisms: physical or chemical adsorption. Physisorption involves the attraction of target molecules onto the surface of pore walls within a sorbent with high surface area, facilitated by van der Waals forces.[11] The heat of adsorption in physisorption is relatively low, only slightly exceeding the heat of sublimation of the adsorbate. In chemisorption, the target gas undergoes a covalent chemical reaction to bind to specific sites on the sorbent, resulting in a significantly higher heat of adsorption that is approximately equivalent to the heat of the reaction.[11] Notable adsorbents in physical adsorption include zeolites, activated carbon, alumina, and metal–organic frameworks.[12] Their performance can be notably reduced by high humidity and elevated temperatures, especially in the cases of activated carbon and zeolites.[4,13] MOFs offer the advantage of being highly flexible when it comes to their shape, pore structure, pore size, and surface properties.[11] Like most sorbents, their sorption capacity and selectivity are influenced by temperature and humidity. In general, MOFs are better suited for storage purposes rather than for the capture or separation of CO_2.[11,14] The heat of adsorption of carbon dioxide on these types of sorbents ranges from −25 to −40 kJ per mole, close to the heat of sublimation (~25 kJ per mole).[11,12] This low heat of adsorption reduces the amount of energy needed to desorb a given quantity of carbon dioxide. Conversely, solid sorbents that capture carbon dioxide *via* a chemical process, such as bonding with an amine grafted or coated onto the sorbent's surface, exhibit significantly higher heats of adsorption. Depending on the specific amine employed, the heat of adsorption typically ranges between −60 and −100 kJ mol^{-1}.[11]

This article reports perovskite oxides as a new family of solid sorbents for CO_2 capture. Perovskites are appealing due to their remarkable stability and high compositional and structural flexibility, allowing for tunability in terms of their surface and bulk properties.[15–19] Despite their flexibility and applications in thermal and electro catalysis, ceramic membranes, sensing, *etc.*[20–22] perovskite oxides have not been explored as CO_2 sorbents at low temperatures. Meanwhile, a number of previous studies have shown that alkali earth cations in perovskite oxides tend to enrich on the perovskite surface.[23–28] This can lead to strong interaction with CO_2.[23–28] Although formation of bulk carbonate phases is not desirable, surface interactions between CO_2 and surface alkali earth cations, whose coordination environment may be tunable by varying the perovskite composition, can offer interesting opportunities. In our current investigation, we utilized $Sr_xLa_{1-x}FeO_3$ (where x = 0, 0.2, 0.5, and 0.7) as a model system to illustrate how altering the A-site composition of perovskite oxide can significantly affect the behavior of CO_2 adsorption and desorption. This variation allowed us to achieve adjustable CO_2 release within a temperature range spanning from 180 to over 500 °C. We established a strong correlation between the surface area of the oxide and its sorption capacity. By employing an electrospinning method to create nanofibers known for their high surface areas,[29,30] we successfully increased the surface area from 3 to 5 $m^2\ g^{-1}$ (achieved through a salt-assisted reactive grinding method) to approximately 30 $m^2\ g^{-1}$, resulting in a significant increase in the CO_2 capture capacity (up to 0.68 wt%). This investigation highlights the potential of perovskite oxides as a customizable category of CO_2 sorbent materials, with the possibility of further enhancing their surface area for practical applications in CO_2 capture and combined CO_2 capture and utilization.

2 Experimental section

2.1 Synthesis of $Sr_xLa_{1-x}FeO_3$ sorbents

Solid-state method. Perovskite oxides were synthesized using a solid-state method. In a typical synthesis of $Sr_xLa_{1-x}FeO_3$, we weighed stoichiometric amounts of $SrCO_3$, La_2O_3, and Fe_2O_3 and placed them in a stainless-steel sample jar. Subsequently, we added 3 mm ZrO_2 beads to the jar in a mass ratio of 5 : 1. To prevent the powders from adhering to the stainless-steel sample jar, we added 9 mL of ethanol (>99 vol% purity) to the mixture. The mixture was then ball-milled at 1200 rpm for 3 hours. Afterward, we dried the resulting wet mixture in the stainless-steel sample jar at 130 °C for 30 minutes to remove the ethanol. Following this step, the powder mixture was separated from the ZrO_2 beads and calcined at 1000 °C in a muffle furnace for 10 hours to obtain the perovskite structure. Both the heating and cooling rates were set at 3 °C min^{-1}. Finally, the perovskite samples were sieved to particle sizes below 250 μm for TGA testing. To enhance the surface area of perovskite materials, we employed the salt-grinding method, aiming to create a porous structure. The perovskite was blended with K_2CO_3 and 3 mm ZrO_2 beads inside a stainless-steel sample jar, maintaining a specific mass ratio. Subsequently, the jar underwent ball milling at 1200 rpm for 24 hours, utilizing a high-energy ball mill to augment porosity. The resultant powder mixtures were subjected to a water rinse to eliminate K_2CO_3. Subsequently, the remaining moist particles were dried in an oven at 130 °C to yield the high-porosity perovskite materials.

Electrospinning method. The synthesis of $Sr_{0.2}La_{0.8}FeO_3$ perovskite oxide was carried out through the electrospinning method using metal precursors and a polymer solution. Details of this technique are established elsewhere.[29,30] Briefly, a polymer solution is pumped through a syringe in this method. The ejected solution is subjected to an electric field causing it to elongate into nanofibers. These nanofibers are collected as a nonwoven fibrous web on a collector placed at a specified distance from the syringe tip.[31] In our case, a solution was prepared by fully dissolving $La(NO_3)_3 \cdot 6H_2O$, $Sr(NO_3)_2$, and $Fe(NO_3)_3 \cdot 9H_2O$ in a mixture of H_2O, C_2H_5OH (ethanol), and DMF (dimethylformamide) in a 2 : 5 : 5 mass ratio. Additionally, 15.5 wt% PVP (polyvinylpyrrolidone) was added to the solution. The electrospinning process was conducted with a distance of 15 cm between the needle tip of the syringe and a grounded aluminum foil collector. An applied voltage of 20 kV was used, which was generated by a custom-made D.C. power supply. To control the injection rate, a syringe pump (New Era Pump System Inc., Model no. NE-300) was employed, maintaining a rate of 0.5 mL min^{-1}. Following the electrospinning step, the resulting fibers were dried at 80 °C in an oven overnight and then collected. To obtain the $Sr_{0.2}La_{0.8}FeO_3$ perovskite oxide,

the collected fibers were subjected to calcination at 650 °C for 3 hours, employing a heating rate of 3 °C min^{-1} in air. It should be noted that while our approach here entailed a lab scale setup, industrial production lines for electrospinning have been designed and implemented industrially, enabling the large-scale manufacturing of electrospun nanofibers for applications such as air and water filtration, biomedical devices, and energy storage systems. Many of these approaches use multi-needle or nozzle-less systems, incorporating real-time monitoring for quality assurance and developing solvent-free or environmentally friendly methods to reduce costs and minimize environmental impact.[32,33]

2.2 Sorbent evaluation

The CO_2 adsorption capacity of $Sr_xLa_{1-x}FeO_3$ was investigated using a TA Instruments SDT 650 thermogravimetric analyzer (TGA) at a temperature of 35 °C. Samples weighing between 30 and 40 mg were loaded into an Al_2O_3 crucible with a 6.5 mm inner diameter and subsequently placed inside the TGA apparatus. The samples were then subjected to heating at a rate of 20 °C per minute until reaching 550 °C under an Ar atmosphere with a purity of 99.999% and a flow rate of 200 mL min^{-1}. This heating step was maintained for 60 minutes to eliminate any adsorbed species. Following the cooling of the samples to the desired analysis temperature, a 60-minute equilibration period was allowed before switching the gas flow to a mixture comprising 10% CO_2 and 90% Ar at a flow rate of 200 mL min^{-1}. This CO_2 exposure was conducted for a duration of 30 minutes. Subsequently, to initiate the desorption step and release CO_2 species from the surface, the temperature was increased, and pure argon was employed. Cycle adsorption and desorption stability experiments were conducted under similar conditions.

2.3 Sorbent characterization

X-ray diffraction analysis (XRD). The crystal structures of the samples were determined using an Empyrean PANalytical X-ray diffraction (XRD) instrument, which utilized Cu-Kα radiation with a wavelength (λ) of 1.5406 Å. The XRD apparatus was operated at 45 kilovolts (kV) and 40 milliamperes (mA). The scanning process covered a range of 2θ values from 10° to 90°, employing a step size of 0.0262° for each measurement and a holding time of 0.2 seconds per step. To identify the XRD phases present in the samples, Highscore Plus software was employed.

Surface area measurement. The Brunauer–Emmett–Teller (BET) surface areas (denoted as S_{BET}) and pore volumes of the samples were assessed using nitrogen sorption analysis, which was carried out with a Micromeritics ASAP 2020 instrument at a temperature of 77 K. Before commencing the measurements, the samples underwent a degassing process, reducing the pressure to less than 5 mmHg, and were heated at 200 °C for a duration of 10 hours to remove any residual gases and impurities. The determination of S_{BET} followed the multipoint BET method within the pressure range of 0 to 120 kPa, allowing for comprehensive characterization of the samples' surface properties and porosity.

CO_2 adsorption isotherms. The study involved examining the adsorption of CO_2 at low temperatures of 0 °C and 25 °C, employing a precise Micrometrics ASAP 2020 instrument. To ensure the accuracy of the measurements, a meticulous sample preparation procedure was followed. Initially, the samples were subjected to a rigorous degassing process, which effectively reduced the pressure within the system to less than 5 mmHg. Subsequently, these samples were carefully heated to a temperature of 200 °C for a duration of 10 hours. This thermal treatment was essential to eliminate any residual gases and impurities, thereby ensuring the purity of the samples. Once the samples were suitably prepared, the determination of CO_2 adsorption was carried out across a wide range of pressure conditions, spanning from 0 to 120 kPa.

Electron microscopy. High-resolution transmission electron microscopy (HRTEM) and scanning TEM high-angle annular dark-field (STEM-HAADF) equipped with energy dispersive X-ray (EDX) tomography to survey elemental mappings were employed to unveil morphology and elemental composition (FischerScientific Talos, 200 kV). Additionally, it was equipped with a specialized liquid nitrogen-cooled energy-dispersive X-ray spectroscopy (EDS) detector to facilitate elemental analysis. To prepare the samples for analysis, they were initially transformed into fine powders. Subsequently, these powders were dispersed in ethanol using ultrasonication, ensuring an even distribution. The resulting suspension was then carefully deposited onto a Cu grid coated with holey carbon. Finally, the prepared samples were left to air dry under standard ambient conditions before HRTEM analysis was performed.

The surface morphology of the catalyst was analyzed using a Thermo Fisher Scientific Verios 460L Field Emission Scanning Electron Microscope (SEM) operating at 2 kV. Samples were mounted onto conductive carbon tape, and secondary electron images were captured without the application of any coating.

X-ray photoelectron spectroscopy (XPS). XPS spectra were obtained using the following parameters: a current of 10 mA and an accelerating voltage of 15 kV. The data acquisition involved a pass energy of 20 eV and a step size of 0.1 eV. Subsequently, peak deconvolution was carried out utilizing Casa XPS software, developed by Casa Software Ltd in the United Kingdom. This process included the application of a Shirley background subtraction method and the use of mixed Gaussian–Lorentzian functions to enhance peak resolution. Furthermore, the binding energies in the obtained spectra were calibrated with reference to the C 1s peak, which was assigned a value of 285 eV.

Fourier-transform infrared spectroscopy (FTIR). To obtain *ex situ* IR data, we employed FTIR spectroscopy using a Thermo Fisher Nicolet iS50 ATR instrument. The process began by introducing the freshly prepared sample into an *ex situ* cell. To establish the background spectrum, the instrument recorded the spectrum from the fresh sample, which was subsequently automatically subtracted from the sample spectrum. For the sample spectrum, we subjected the sample to a pre-treatment phase within a TGA (Thermogravimetric Analyzer). During this phase, we introduced pure Ar (99.99%) as the carrier gas.

Following this, we conducted the first cycle of CO_2 adsorption using a gas mixture of CO_2/Ar (10% CO_2, 90% Ar) at a flow rate of 200 mL min^{-1}. This adsorption process was carried out for a duration of 30 minutes at a temperature of 35 °C. Subsequently, we stopped the TGA and transferred the treated sample to an *ex situ* IR setup to collect the sample spectrum.

In order to collect *in situ* IR data, FTIR spectroscopy was employed using a Thermo Fisher Nicolet iS50 FTIR, which was equipped with a DiffusIR sample chamber from Pike Technologies. The process began by loading the sample into an *in situ* cell and purging it with Ar gas at 600 °C for a duration of 30 minutes. After this step, the sample was cooled to a temperature of 25 °C. To obtain the background spectrum, the instrument was used to collect the spectrum in an Ar stream at 25 °C, which was then automatically subtracted from the sample spectrum. CO_2 reaction gas was introduced into the reaction cell at a flow rate of 40 mL min^{-1}, and spectra were collected repeatedly until the spectrum curve stabilized.

3 Results and discussion

3.1 Sorbent phase purity and the effect of preparation methods on sorbent surface areas

To determine the effect of A-site compositions on perovskites' CO_2 sorption properties, a simple solid state synthesis method was adopted first to prepare the perovskite samples for screening purpose. This is followed with X-ray diffraction analysis (XRD) to confirm their phase purity. As shown in Fig. 1a, the XRD patterns for all the synthesized samples exhibited well-defined diffraction peaks, signifying their phase purity.

One of the key challenges associated with the use of perovskites as adsorbents for CO_2 capture is their inherently low surface area, which consequently results in a limited adsorption capacity. To address this limitation, we adopted two strategies, *i.e.* reactive grinding and creating nanofibrous structure *via* electrospinning, to increase their surface area. Using potassium as an alkali additive in reactive grinding increases surface area and adsorption capacity. Electrospinning with surfactants and templates, followed by calcination, creates perovskite oxides with higher surface areas and potentially controllable nanostructures.

Table 1 The results of the BET analysis for perovskite were compared before and after the processes of grinding and electrospinning

Sample	S_{BET} (m^2 g^{-1})	V_p (cm^3 g^{-1})	S_p (Å)
$LaFeO_3$	3.43	0.0091	128.3
$Sr_{0.2}La_{0.8}FeO_3$	2.38	0.0076	143
$Sr_{0.5}La_{0.5}FeO_3$	3.55	0.0079	101.3
$Sr_{0.7}La_{0.3}FeO_3$	2.93	0.0063	108.8
LaFe-grind	15.76	0.075	164.5
$Sr_{0.2}La_{0.8}FeO_3$-grind	15.56	0.098	213
$Sr_{0.5}La_{0.5}FeO_3$-grind	23.36	0.132	206
$Sr_{0.7}La_{0.3}FeO_3$-grind	14.18	0.079	201
$Sr_{0.2}La_{0.8}FeO_3$-electrospun	29.55	0.119	143.5

Table 1 summarizes the BET surface areas of $Sr_xLa_{1-x}FeO_3$ (x = 0, 0.2, 0.5, 0.7) perovskite oxides before and after grinding with salt. As can be seen, before grinding, the perovskite's surface area averaged 3 to 5 m^2 g^{-1}. In comparison, the surface area increased nearly five-fold on average after reactive grinding. To further enhance the surface area of the perovskite, we employed the electrospinning technique. The BET results demonstrated the efficacy of this approach, with the surface area of the as-prepared $Sr_{0.2}La_{0.8}FeO_3$ increasing to nearly 30 m^2 g^{-1}. This finding underscores the efficacy of electrospinning as a synthesis approach for enhancing the surface area. As illustrated in Fig. 1b and c, following the reactive grinding and electrospinning process, the perovskite materials have maintained their phase purity.

3.2 Tunability of sorbents' surface properties for CO_2 adsorption

The Sr percentage in the perovskite A-site is fully adjustable in $Sr_xLa_{1-x}FeO_3$ perovskite oxides. Given the high basicity of Sr^{2+}, adjusting this ratio significantly influences the surface characteristics and sorption properties of the sorbents. Our research demonstrates that increasing the amount of strontium in the A-

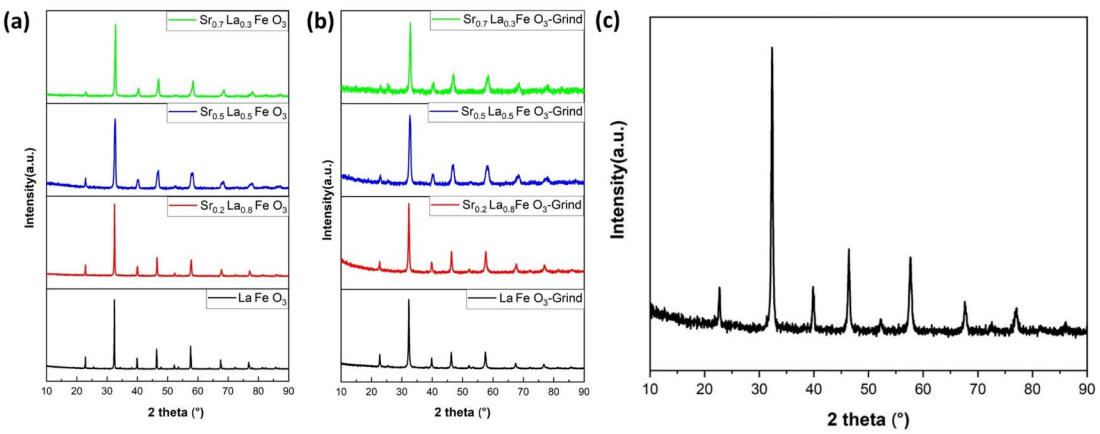

Fig. 1 XRD results of $Sr_xLa_{1-x}FeO_3$ (x = 0, 0.2, 0.5, 0.7) perovskite oxide. (a) Before grinding with salt and (b) after grinding with salt. (c) XRD result of $Sr_{0.2}La_{0.8}FeO_3$ (electrospun).

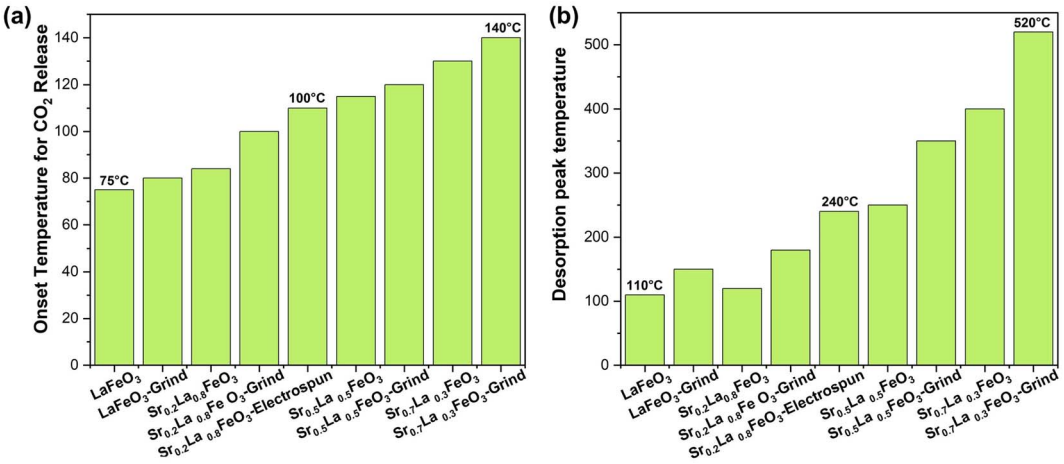

Fig. 2 TGA results of $Sr_xLa_{1-x}FeO_3$ perovskite oxide. (a) Onset temperature for CO_2 release of $Sr_xLa_{1-x}FeO_3$ perovskite oxide ($x = 0$, 0.2, 0.5, 0.7). (b) Desorption peak temperature of $Sr_xLa_{1-x}FeO_3$ perovskite oxide ($x = 0$, 0.2, 0.5, 0.7).

site makes the perovskite surface progressively more basic, facilitating the formation of more strontium carbonate and raising the desorption temperature, as shown in Fig. 2a. The TGA results indicate that the onset temperature for CO_2 desorption, determined based on the second order derivative of the weight as a function of temperature, increased with increasing strontium content from 75 to 140 °C. Meanwhile, the peak desorption temperature also varied significantly with the strontium content: the $Sr_{0.2}La_{0.8}FeO_3$ sample desorbs at around 120 °C (180 °C after grinding, likely due to residual potassium), while the $Sr_{0.7}La_{0.3}FeO_3$ sample desorbs at over 500 °C (Fig. 2b). Thus, increasing strontium in the A-site primarily elevates the desorption temperature, with only a modest impact on adsorption capacity. Since a lower desorption temperature leads to lower energy consumption, we selected the sample with the lowest strontium content and then focused on enhancing the perovskite's surface area to improve carbon dioxide adsorption.

3.3 Effect of the synthesis method on sorption capacity

Although sorbents prepared *via* SSR showed excellent phase purity and tunable sorption properties, their sorption capacities are rather limited (~0.05 wt%). This is largely due to their low surface areas which are intrinsic to perovskite oxides. As shown in Table 1. We chose the $Sr_{0.2}La_{0.8}FeO_3$ sample and increased its surface area by grinding it with potassium carbonate. Before grinding, the perovskite demonstrates an adsorption capacity of ~0.05 wt%, as revealed by TGA analysis. Subsequent to the grinding process, the adsorption capacity more than tripled to ~0.18 wt%. Fig. 3a shows the cycling stability of the sorbent. As can be seen, the adsorption capacity remained constant throughout the test, confirming its durability.

To further enhance the surface area of the perovskite, we employed the electrospinning technique. In this method, our objective is to determine the optimal calcination temperature that maximizes both phase purity and surface area. We conducted *in situ* XRD across a temperature range spanning from 400 to 700 °C. At 700 °C, we observed a surface area of approximately 17 $m^2\ g^{-1}$, accompanied by the presence of a pure phase. However, at 550 °C, while we achieved a surface area of around 35 $m^2\ g^{-1}$, we did not attain phase purity. It was therefore determined that the most suitable calcination temperature is 650 °C, as it allows us to achieve both phase purity and a high surface area (Fig. 3b). We conducted a cyclic experiment using TGA on $Sr_{0.2}La_{0.8}FeO_3$ synthesized through the electrospinning method. This material exhibited excellent stability throughout the repeated cycles of adsorption and desorption (Fig. 3c and S1a†) at a low concentration of carbon dioxide (0.4 vol% CO_2 balance Ar). As shown in Fig. 3c, the sample demonstrates notable stability, with its adsorption capacity exhibiting consistency across 55 cycles. This observation underscores the effectiveness of the $Sr_{0.2}La_{0.8}FeO_3$ sorbent (synthesized *via* electrospinning).

As can be seen from Fig. 3d, sorption capacity is directly related to the sorbent surface area. In fact, sorbent capacities are proportional to their surface areas for the $Sr_{0.2}La_{0.8}FeO_3$ samples prepared by SSR and reactive grinding. However, the electrospun sample does not follow this linear correlation: its sorption capacity (~0.68 wt%) is more than three times greater than that achieved through the reactive grinding method, although its surface area only doubled. This variance in adsorption capacity is therefore likely attributable to differences in both surface area and the nature of the surface adsorption sites. The difference in surface properties is further discussed in the next section.

3.4 Effect of the synthesis method on sorbents' surface and sorption properties

The SEM image in Fig. 4a depicts the electrospun nanofibrous mat before the calcination process of $Sr_{0.2}La_{0.8}FeO_3$, confirming that the electrospinning conditions indeed produce fibers that are devoid of aggregates, demonstrating a homogeneous structure.[34] However, post-calcination, the fibrous mat is broken up, revealing a rod-like or short nanofiber shape, as evidenced in Fig. 4b. This is akin to shearing nanofiber

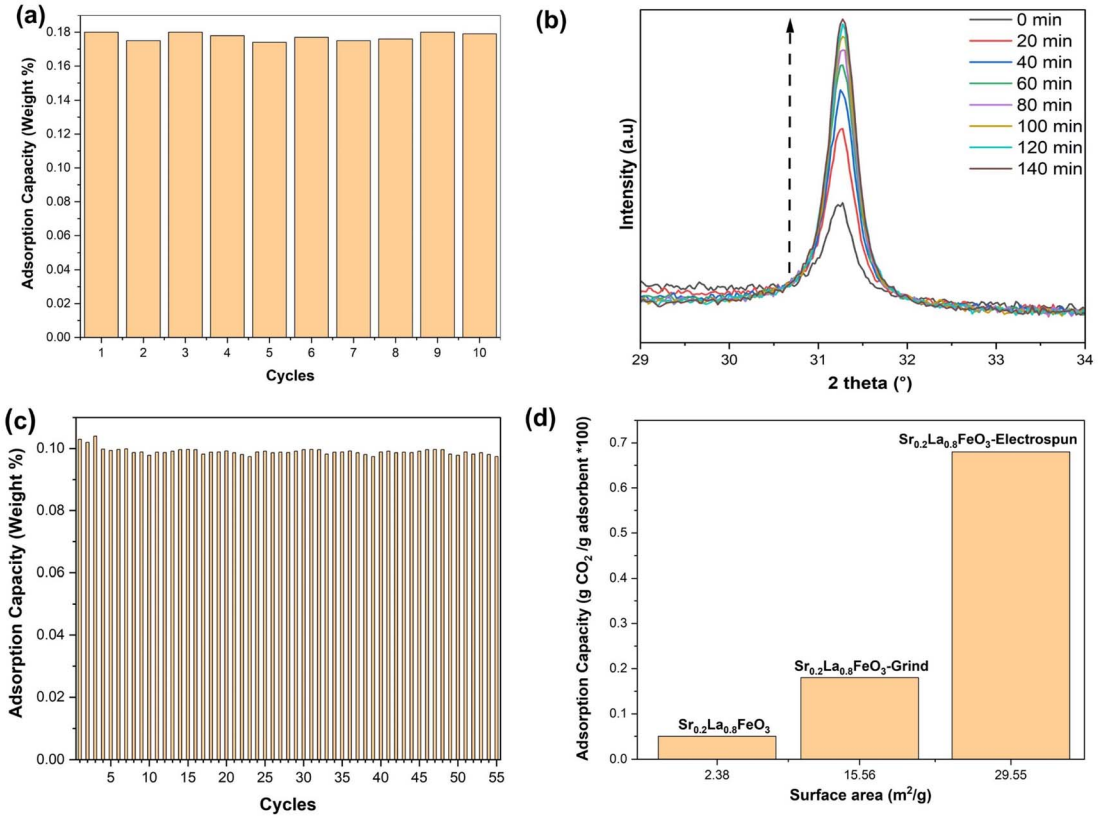

Fig. 3 (a) Cyclic CO_2 uptake of $Sr_{0.2}La_{0.8}FeO_3$ (reactive grinding) at 35 °C using CO_2/Ar (10/90) *via* a gravimetric method. (b) *In situ* XRD analysis of $Sr_{0.2}La_{0.8}FeO_3$ (electrospun) at 650 °C over varying exposure times. (c) Cyclic CO_2 uptake of $Sr_{0.2}La_{0.8}FeO_3$ (electrospun) at 35 °C using 0.4% CO_2 *via* a gravimetric method. (d) Correlation between surface area and adsorption capacity for $Sr_{0.2}La_{0.8}FeO_3$ (grinding with salt) and $Sr_{0.2}La_{0.8}FeO_3$ (electrospun).

dispersions to break them into smaller fibers that still provide a high surface area.[35,36] This transformation occurs during the calcination process, wherein the decomposition of polyvinylpyrrolidone (PVP) takes place and the metal precursors stabilize to form a distinctive nanorod structure (Fig. 4c).[37] To further characterize the material, an elemental analysis was performed using energy-dispersive X-ray spectroscopy (EDS), resulting in the distribution of atoms represented in the color map depicted in Fig. 4d. The EDS element images confirm the presence of all elements within the $Sr_{0.2}La_{0.8}FeO_3$ composition, illustrating their well-dispersed distribution throughout the nanorod structure.[37] The high aspect ratios of the nanorod structure result in a greater surface area compared to cluster materials obtained through reactive grinding, as shown in the TEM images of ground materials in Fig. S2.† In addition to offering more active sites for CO_2 adsorption, the change in morphology and hence surface termination/elemental compositions can potentially alter the surface adsorption chemistry, as elaborated next.

XPS analysis was conducted to assess the near surface elemental distribution of the samples prepared *via* electrospinning and reactive grinding methods. According to elemental composition analysis *via* XPS (Fig. 4e), the atomic percentages (carbon and oxygen free basis) are as follows: for $Sr_{0.2}La_{0.8}FeO_3$ (synthesized *via* reactive grinding): the composition is 7.84% for Sr, 31.03% for La, and 61.24% for Fe. For $Sr_{0.2}La_{0.8}FeO_3$ (synthesized *via* electrospinning), the composition is 6.65% for Sr, 55.09% for La, and 38.25% for Fe. These results suggest distinct elemental distributions between the two synthesis methods. Notably, electrospinning results in higher surface concentrations of A site cations, *i.e.* Sr and La, whereas the grinding method shows a higher percentage of Fe. Another interesting aspect is that the electrospun sample exhibited a significantly higher near surface La/Sr ratio (~8.3) than the reactive ground sample (~4). In fact, the near surface Sr concentration is higher in the reactive ground sample (7.84%) than that in the electrospun sample (6.65%). This points to (a) the CO_2 sorption capacity may directly correlate with the surface concentration of A-site cations; (b) La is likely to be responsible for a notable fraction of the observed CO_2 sorption. The latter is somewhat surprising given that Sr was originally envisioned as the active site for CO_2 sorption.

The O 1s spectra for both electrospinning and grinding exhibit two distinct peaks (Fig. 4f). The peak at the lower binding energy can be attributed to lattice oxygen species (O^{2-}),[38–41] whereas the high binding energy peak is attributable to oxygen associated with carbonates[42] or hydroxyls.[43] As can be seen, the electrospun sample shows a weaker carbonate peak (high B.E. to low B.E. peak area ratio = 2/3) compared to the ground sample (peak area ratio = 1/1). Further analysis of the Sr

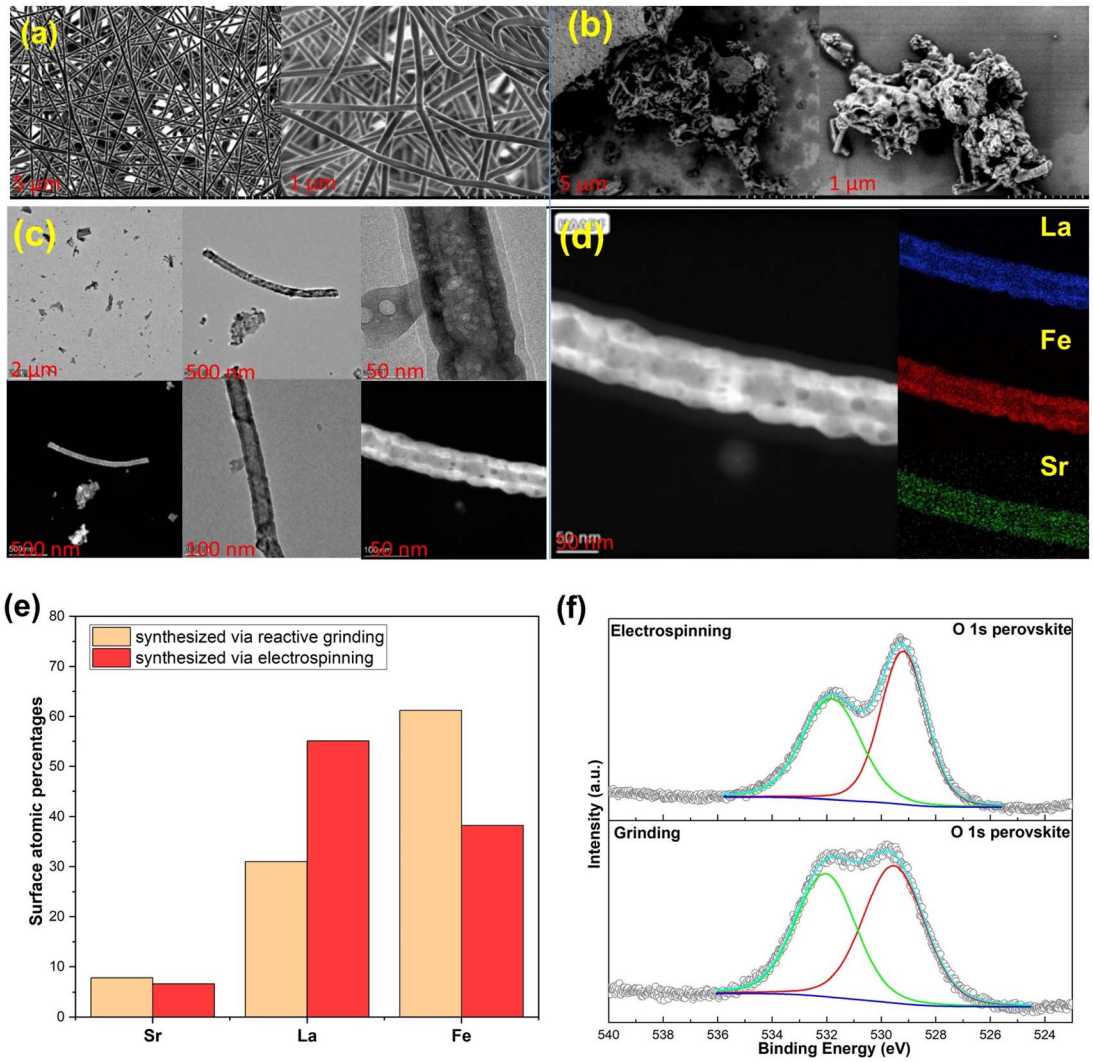

Fig. 4 (a) SEM image of $Sr_{0.2}La_{0.8}FeO_3$ prepared by electrospinning before calcination; (b) post-calcination; (c) TEM images of the electrospun sample; (d) corresponding elemental mapping by EDS; (e) comparison of the XPS derived near surface atomic surface percentages between samples prepared *via* electrospinning and grinding methods; (f) comparisons of the O 1s spectra of the electrospun and reactive ground samples.

3d region confirms the presence of strontium carbonate ($SrCO_3$) on both samples (Fig. S3 and S4†). Regarding the Sr $3d_{5/2}$ region, the broad peak suggests the presence of Sr(II) in various chemical environments. Typically, the dominant peak at 134.46 eV for the electrospinning method and 134.23 eV for the reactive grinding method are attributed to $SrCO_3$. Additionally, the peak at around 132.37 eV for the reactive grinding method and 132.71 eV for the electrospinning method confirm the presence of strontium oxide (SrO) within the perovskite lattice.[44] On the other hand, in the La 3d region, the binding energies observed at 834.19 eV (La $3d_{5/2}$) and 838.1 eV (La $3d_{3/2}$) for the reactive grinding method and 833.92 eV (La $3d_{5/2}$) and 837.78 eV (La $3d_{3/2}$) for the electrospinning method align with the known values for La(III) in similar perovskite structures. These peaks likely correspond to La(III) oxide or hydroxide.[44] These results indicate that the high basicity of the Sr cation may lead to the formation of stable carbonates that are difficult to regeneration/decompose. In comparison, La cations would be largely available for reversible CO_2 sorption/desorption.

To further clarify the role of surface A-site cations, the adsorption enthalpies of the two sorbents were also measured. This involved calculating the isosteric heat of CO_2 adsorption through the utilization of the Clausius–Clapeyron equivalent adsorption heat equation.[45]

$$q_{st} = RT_1T_2\frac{\ln\left(\frac{p_1}{p_2}\right)}{T_2 - T_1} \quad (1)$$

The isosteric heat of adsorption (q_{st}) is calculated using the formula, where R represents the universal gas constant (8.314 J mol^{-1} K^{-1}), T ($T_1 = 298$ K; $T_2 = 273$ K) denotes the adsorption temperature, and P is the adsorption pressure. The q_{st} values for the prepared adsorbents are determined based on the CO_2 adsorption data obtained at 0 and 25 °C. CO_2 adsorption was

carried out from 0 to 120 kPa, as shown in Fig. 5a and b. We note that in the case of adsorption isotherm measurement, the surface area normalized adsorption capacities for the electrospun and ground samples are similar. In contrast, the TGA data indicated that the electrospun sample exhibited significantly higher surface normalized CO_2 sorption capacity (nearly 100% higher than that of the ground sample). This is due to differences in experimental conditions: the TGA measurement was performed to determine the reversible sorption capacity under temperature swings and at a relatively low CO_2 partial pressure (0.1 atm). In contrast, the adsorption isotherm was obtained at low temperatures for up to 1.2 atm of CO_2. Since the samples were pretreated at a high temperature to decompose the stable carbonates prior to the isothermal measurement, it is quite possible that some of the stable carbonates that formed during the isothermal measurement would not contribute to the reversible sorption capacity. Additional TGA tests further confirmed this hypothesis as the reactive ground sample

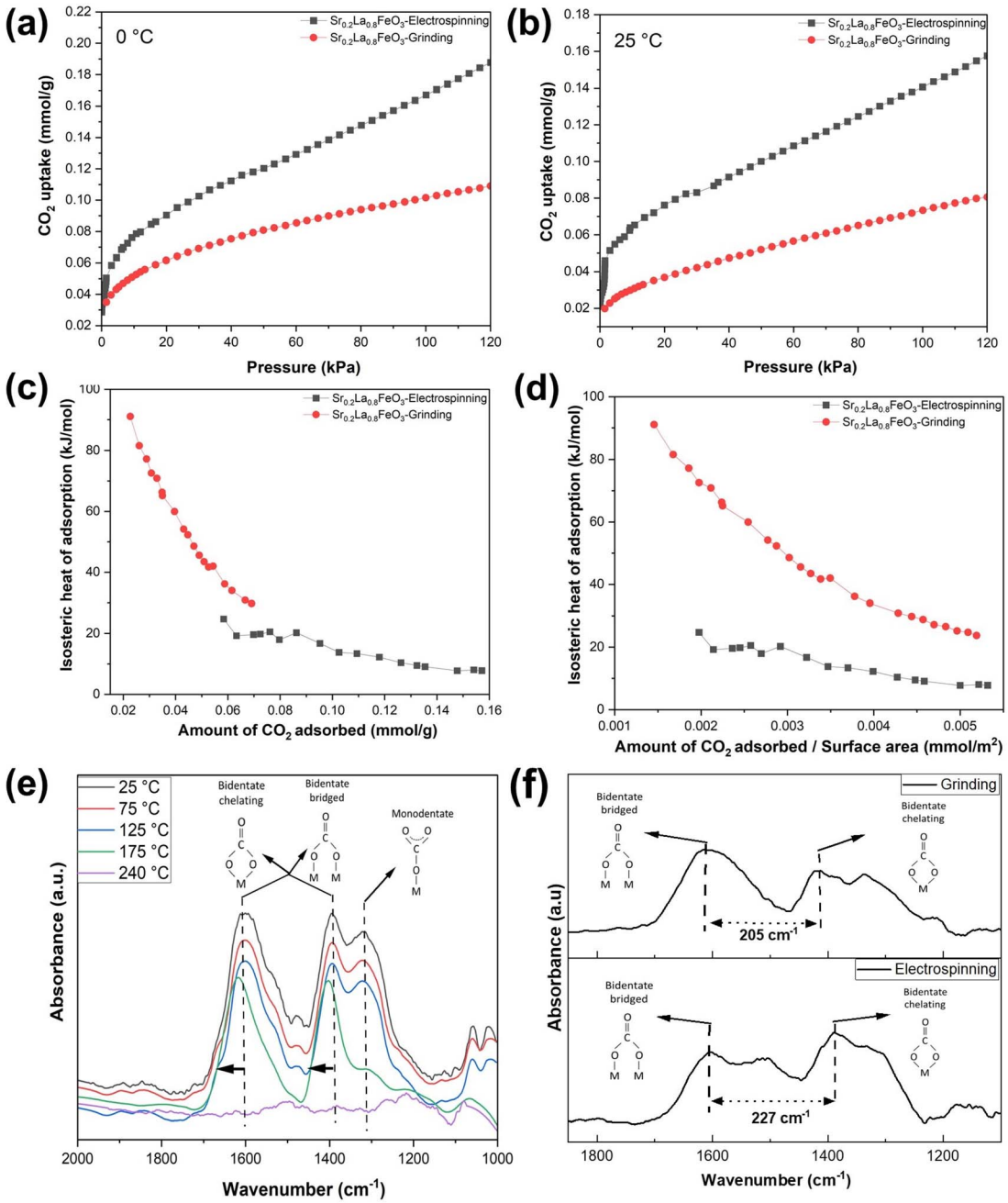

Fig. 5 (a and b) CO_2 adsorption isotherms of $Sr_{0.2}La_{0.8}FeO_3$ at 0 and 25 °C. (c) CO_2 isosteric heats of adsorption. (d) Comparison of isosteric heat of adsorption *vs.* adsorption capacity per surface area for electrospun and ground samples. (e) *In situ* IR spectra of CO_2 adsorbed on $Sr_{0.2}La_{0.8}FeO_3$ (electrospinning) monitored as a function of temperature. (f) *In situ* IR spectra of CO_2 adsorbed on electrospun and ground $Sr_{0.2}La_{0.8}FeO_3$ at 25 °C.

showed a significantly higher amount of stable carbonates that act as a spectator phase and do not contribute to the usable CO_2 capacity under the standard adsorption/desorption conditions (Fig. S6†).

For electrospun $Sr_{0.2}La_{0.8}FeO_3$ at adsorption capacities below 0.0375 mmol g^{-1}, it is difficult to accurately determine the heat of adsorption due to instrumentation limitations in measuring CO_2 uptake at low pressures (Fig. S7a and b†). We note that this low-pressure limitation is not an issue for the ground sample since it requires significantly higher CO_2 partial pressure to achieve the sample adsorption capacity. That said, based on two sets of measurements for the electrospun sample in the low-pressure range (Fig. S7c†), the heat of adsorption for the electrospun sample was approximately 85 kJ mol^{-1} at the lowest measurable pressure (corresponding to ~0.028 mmol g^{-1} CO_2 uptake). Between 0.028 and 0.035 mmol g^{-1}, the heat capacity steadily dropped along with an increase in CO_2 uptake, and the average heat of adsorption within this range is ~70 kJ mol^{-1}, corresponding to chemisorption. This indicates a strong adsorption affinity, with both data sets clearly supporting a chemisorption process characterized by adsorption enthalpies exceeding 60 kJ mol^{-1}. Conversely, for adsorption capacities beyond this threshold, the adsorption enthalpies quickly decrease to below 40 kJ mol^{-1}, indicating physisorption. Overall, the q_{st} value shows a noticeable decline as adsorption progresses, eventually stabilizing nearly 10 kJ mol^{-1} for the electrospun $Sr_{0.2}La_{0.8}FeO_3$. This phenomenon occurs likely because CO_2 would preferentially adsorb on stronger adsorption sites, *e.g.* undercoordinated Sr–O sites. For $Sr_{0.2}La_{0.8}FeO_3$ synthesized *via* reactive grinding, the majority of its adsorption capacity corresponds to chemisorption, with physisorption accounting for only a small fraction of its overall adsorption. The significantly different enthalpy of adsorption profiles between the two samples can potentially be explained by the difference in near surface cation compositions. The XPS results indicate that the electrospun sample has a higher concentration of La near the surface, which acts as the adsorption site and exhibits lower adsorption energy than Sr. On the other hand, in the ground sample, the high Sr concentration leads to strong adsorption energy. However, a notable fraction of the undercoordinated Sr–O sites would contribute to the formation of stable carbonates that do not contribute to usable CO_2 sorption in a practical thermal swing adsorption process, as indicated from the TGA measurements.

To better understand the difference in the adsorption process between the two samples, we calculated the potential site densities on the 111 and 001 surfaces of the electrospun and ground samples and compared these with the experimentally measured adsorption capacity. In our calculations, we assumed that the entire surface could adsorb CO_2 molecules, consistent with monolayer adsorption, using a cubic structure with an approximate distance of 6.7 Å between A-site cations. The calculated adsorption capacities per surface area, based on these assumptions, are approximately 0.0041 mmol CO_2 per m^2 for the 001 surface and 0.00429 mmol CO_2 per m^2 for the 111 surface. The experimental adsorption capacities per surface area of $Sr_{0.2}La_{0.8}FeO_3$ synthesized *via* electrospinning and grinding are around 0.0053 mmol CO_2 per m^2 and 0.0051 mmol CO_2 per m^2, respectively. Based on Fig. 5d, comparing the experimental and calculated adsorption capacities per surface area indicates that both samples exhibit monolayer adsorption.

To unveil the disparity in the interaction between CO_2 molecules and adsorption sites, FTIR was conducted for both samples. Fig. 5e shows the *in situ* FTIR spectra of $Sr_{0.2}La_{0.8}FeO_3$ (electrospinning) at increasing temperature, measured immediately after 10% CO_2 pulses. At each temperature level, the FTIR results in Fig. 5e confirm the presence of both monodentate and bidentate carbonate species. As the temperature increases, the absorbance intensity decreases, indicating a decrease in carbonate content. Notably, beyond 175 °C, one of the monodentate carbonate peaks diminishes, reflecting its weaker bonding compared to bidentate carbonate. This suggests that bidentate adsorption dominates at low CO_2 coverage. With increasing CO_2 coverage, some bidentate species are transformed into monodentate configuration. The disappearance of the carbonate peaks at 240 °C is consistent with the TGA measurements, which showed an onset temperature for CO_2 desorption at 100 °C and a peak desorption temperature of 240 °C. This further confirms that the high near surface La concentration in the electrospun sample inhibits the formation of stable carbonate species and enhances the reversibility of the CO_2 sorption/desorption. These findings also correspond well with the XPS results and enthalpy of adsorption measurements for the electrospun sample.

To compare the binding of CO_2 on the surface of the electrospun and ground samples, we performed the *in situ* analysis with 10% CO_2 balance Ar flowing at a rate of 40 mL min^{-1} operated at 25 °C (Fig. 5f). The carbonate peaks in these two samples exhibit distinct peak locations, stemming from differing surface properties and structures resulting from the electrospinning and grinding methods employed. The greater distance between the bidentate peaks in the electrospun sample compared to the ground sample indicates weaker carbonate species in the electrospun sample.[46] This corroborates well with the isotherm analysis (Fig. 5c and d). Overall, it is evident that the higher surface La concentration in the electrospun sample provides favorable adsorption sites for reversible sorption and desorption of CO_2. On the other hand, a high surface Sr concentration, *e.g.* on the reactive ground sample, would lead to highly stable carbonate species that are not desirable for low temperature CO_2 sorption applications. These findings provide valuable insights into tailoring materials for improved adsorption performance.

4 Conclusions

CO_2 adsorption using solid sorbents offers a promising approach to carbon capture due to low energy requirements, operational simplicity, and high stability. This study introduces perovskite oxides as a tunable family of solid sorbents with exceptional structural and compositional flexibility to optimize sorption thermodynamics and kinetics. Using $Sr_xLa_{1-x}FeO_3$ ($x = 0$, 0.2, 0.5, and 0.7) as a model system, we demonstrated that varying the A-site composition enables a wide range of tunable

CO_2 desorption temperatures (75–500+ °C). A strong correlation between surface area and sorption capacity was also established, along with effective methods to enhance the oxide surface area: a salt-assisted grinding method resulted in samples with 16 $m^2\ g^{-1}$ whereas an electrospinning method enhanced surface areas to ~30 $m^2\ g^{-1}$ from 3–5 $m^2\ g^{-1}$.

Among the synthesized materials, $Sr_{0.2}La_{0.8}FeO_3$ prepared *via* electrospinning exhibited the highest performance, with a moderate desorption temperature (onset: 120 °C and peak: 240 °C) and a sorption capacity of 0.68 wt%. Adsorption isotherm analysis revealed that CO_2 chemisorption dominates at low pressures (0–1 kPa), while physisorption becomes significant at higher pressures. TEM analysis indicated the formation of perovskite nanorods through electrospinning. XPS and (*in situ*) IR characterization studies, coupled with experimental measurements, revealed that near surface La concentrations play a crucial role in reversible CO_2 sorption. The significant over-representation of La on the surface of the electrospun sample compared to other preparation methods led to a superior surface normalized reversible CO_2 sorption capacity.

This study highlights tunable perovskite oxides as a promising new class of CO_2 sorbents. While the demonstrated capacity remains lower than that of typical solid sorbents reported to date (~1.3–14%),[47–52] their high stability and tunability, combined with opportunities for further optimization of surface area and composition, position these oxides as potential candidates for practical applications in CO_2 capture and utilization.

Data availability

Data supporting this article have been included as part of the ESI.†

Author contributions

Seyedamin Razavi: investigation, and writing – original draft. Vahid Rahmanian: conceptualization – review & editing. Runxia Cai: conceptualization – review & editing. Mahe Rukh: conceptualization. Saad Khan: writing – conceptualization, reviewing and editing, supervision. Fanxing Li: conceptualization, writing – review & editing, supervision, project administration, and funding acquisition.

Conflicts of interest

There are no conflicts to declare.

Acknowledgements

This work was supported by the Novo Nordisk Foundation (Grant No. NNF22SA0078767) under the Biocatalyst Interactions with Gases program. We would like to acknowledge Dr Sonja Salmon's helpful comments and suggestions.

References

1 B. N. Firtescu, F. Brinza, M. Grosu, E. M. Doaca and A. A. Siriteanu, *Front. Environ. Sci.*, 2023, **10**, 965841.
2 E. S. Sanz-Perez, C. R. Murdock, S. A. Didas and C. W. Jones, *Chem. Rev.*, 2016, **116**, 11840–11876.
3 D. Welsby, J. Price, S. Pye and P. Ekins, *Nature*, 2021, **597**, 230–234.
4 S. Choi, J. H. Drese and C. W. Jones, *ChemSusChem*, 2009, **2**, 796–854.
5 M. Yates, J. Blanco, P. Avila and M. Martin, *Microporous Mesoporous Mater.*, 2000, **37**, 201–208.
6 B. B. Saha, S. Koyama, I. I. El-Sharkawy, K. Habib, K. Srinivasan and P. Dutta, *J. Chem. Eng. Data*, 2007, **52**, 2419–2424.
7 H. Yang, Z. Xu, M. Fan, R. Gupta, R. B. Slimane, A. E. Bland and I. Wright, *J. Environ. Sci.*, 2008, **20**, 14–27.
8 T. Ashirov and A. Coskun, *Chimia*, 2024, **78**, 415–422.
9 C. W. Jones, *Annu. Rev. Chem. Biomol. Eng.*, 2011, **2**, 31–52.
10 A. Goeppert, M. Czaun, G. S. Prakash and G. A. Olah, *Energy Environ. Sci.*, 2012, **5**, 7833–7853.
11 D. M. Ruthven, S. Farooq and K. S. Knaebel, *Pressure Swing Adsorption*, John Wiley & Sons, 1996.
12 O. Shekhah, Y. Belmabkhout, Z. Chen, V. Guillerm, A. Cairns, K. Adil and M. Eddaoudi, *Nat. Commun.*, 2014, **5**, 4228.
13 F. Brandani and D. M. Ruthven, *Ind. Eng. Chem. Res.*, 2004, **43**, 8339–8344.
14 R. Wu, E. Carrejo, M. S. Reza, E. Woods, S. Razavi, S. Park, F. Li and W. J. Sagues, *Fuel*, 2024, **373**, 132372.
15 L. Brody, M. Rukh, R. Cai, A. Saberi Bosari, R. Schomäcker and F. Li, *J. Phys.: Energy*, 2023, **5**, 035004.
16 R. Cai, K. Yang, X. Wang, M. Rukh, A. S. Bosari, E. Giavedoni, A. Pierce, L. Brody, W. Tang, P. R. Westmoreland and F. Li, *Energy Environ. Sci.*, 2024, **17**, 6279–6290.
17 A. Sayari, Y. Belmabkhout and R. Serna-Guerrero, *Chem. Eng. J.*, 2011, **171**, 760–774.
18 C.-H. Yu, C.-H. Huang and C.-S. Tan, *Aerosol Air Qual. Res.*, 2012, **12**, 745–769.
19 M. Li, M. Zhao, F. Li, W. Zhou, V. K. Peterson, X. Xu, Z. Shao, I. Gentle and Z. Zhu, *Nat. Commun.*, 2017, **8**, 13990.
20 Y. Cao, J. Liang, X. Li, L. Yue, Q. Liu, S. Lu, A. M. Asiri, J. Hu, Y. Luo and X. Sun, *Chem. Commun.*, 2021, **57**, 2343–2355.
21 B. Koo, K. Kim, J. K. Kim, H. Kwon, J. W. Han and W. Jung, *Joule*, 2018, **2**, 1476–1499.
22 M. Rukh, R. Cai, L. Brody and F. Li, *Chem. Eng. J.*, 2024, **501**, 157545.
23 Y. Zhu, W. Zhou, Z. G. Chen, Y. Chen, C. Su, M. O. Tadé and Z. Shao, *Angew. Chem.*, 2015, **127**, 3969–3973.
24 C. Borca, B. Xu, T. Komesu, H.-K. Jeong, M. Liu, S.-H. Liou and P. Dowben, *Surf. Sci.*, 2002, **512**, L346–L352.
25 W. Lee and B. Yildiz, *ECS Trans.*, 2013, **57**, 2115.
26 E. J. Crumlin, E. Mutoro, Z. Liu, M. E. Grass, M. D. Biegalski, Y.-L. Lee, D. Morgan, H. M. Christen, H. Bluhm and Y. Shao-Horn, *Energy Environ. Sci.*, 2012, **5**, 6081–6088.

27 A. Nenning, A. K. Opitz, C. Rameshan, R. Rameshan, R. Blume, M. Hävecker, A. Knop-Gericke, G. n. Rupprechter, B. Klötzer and J. r. Fleig, *J. Phys. Chem. C*, 2016, **120**, 1461–1471.
28 Y. Chen, W. Jung, Z. Cai, J. J. Kim, H. L. Tuller and B. Yildiz, *Energy Environ. Sci.*, 2012, **5**, 7979–7988.
29 C. D. Saquing, J. L. Manasco and S. A. Khan, *Small*, 2009, **5**, 944–951.
30 C. A. Bonino, M. D. Krebs, C. D. Saquing, S. I. Jeong, K. L. Shearer, E. Alsberg and S. A. Khan, *Carbohydr. Polym.*, 2011, **85**, 111–119.
31 B. V. Farias, T. Pirzada, R. Mathew, T. L. Sit, C. Opperman and S. A. Khan, *ACS Sustain. Chem. Eng.*, 2019, **7**, 19848–19856.
32 J. Xue, T. Wu, Y. Dai and Y. Xia, *Chem. Rev.*, 2019, **119**, 5298–5415.
33 G. Zheng, J. Jiang, X. Wang, W. Li, J. Liu, G. Fu and L. Lin, *Mater. Des.*, 2020, **189**.
34 D. Chen and Y. Zhu, *Nanoscale Res. Lett.*, 2017, **12**, 1–5.
35 T. Pirzada, Z. Ashrafi, W. Xie and S. A. Khan, *Adv. Funct. Mater.*, 2019, **30**.
36 V. Rahmanian, M. Z. Ahmad Ebrahim, S. Razavi, M. Abdelmigeed, E. Barbieri, S. Menegatti, G. N. Parsons, F. Li, T. Pirzada and S. A. Khan, *J. Mater. Chem. A*, 2024, **12**, 214–226.
37 Y. Cao, B. Lin, Y. Sun, H. Yang and X. Zhang, *J. Alloys Compd.*, 2015, **624**, 31–39.
38 Y. Teraoka, H.-M. Zhang and N. Yamazoe, *Chem. Lett.*, 2000, **19**, 5.
39 G. Kulkarni, C. Rao and M. Roberts, *J. Phys. Chem.*, 1995, **99**, 3310–3316.
40 A. Carley, M. Roberts and A. Santra, *J. Phys. Chem. B*, 1997, **101**, 9978–9983.
41 J. Fierro and L. G. Tejuca, *Appl. Surf. Sci.*, 1987, **27**, 453–457.
42 T. H. Fleisch, R. F. Hicks and A. T. Bell, *J. Catal.*, 1984, **87**, 398–413.
43 J. Fierro, *Catal. Today*, 1990, **8**, 153–174.
44 X. Xu, W. Wang, W. Zhou and Z. Shao, *Small Methods*, 2018, **2**, 1800071.
45 S. Richard, A. Mitchell, C. Evans, J. Whitaker, A. Thomson and A. Keith, *Greenhouse gas removal methods and their potential UK deployment*, Department for Business, Energy & Industrial Strategy, London, 2021, 120pp.
46 G. Busca and V. Lorenzelli, *Mater. Chem.*, 1982, **7**, 89–126.
47 P. Priyadarshini, G. Rim, C. Rosu, M. Song and C. W. Jones, *ACS Environ. Au*, 2023, **3**, 295–307.
48 G. Rim, P. Priyadarshini, M. Song, Y. Wang, A. Bai, M. J. Realff, R. P. Lively and C. W. Jones, *J. Am. Chem. Soc.*, 2023, **145**, 7190–7204.
49 A. Holewinski, M. A. Sakwa-Novak and C. W. Jones, *J. Am. Chem. Soc.*, 2015, **137**, 11749–11759.
50 M. Zhao, J. Xiao, W. Gao and Q. Wang, *J. Energy Chem.*, 2022, **68**, 401–410.
51 J. Wang, H. Huang, M. Wang, L. Yao, W. Qiao, D. Long and L. Ling, *Ind. Eng. Chem. Res.*, 2015, **54**, 5319–5327.
52 X. Zhu, W. Xie, J. Wu, Y. Miao, C. Xiang, C. Chen, B. Ge, Z. Gan, F. Yang, M. Zhang, D. O'Hare, J. Li, T. Ge and R. Wang, *Chem. Soc. Rev.*, 2022, **51**, 6574–6651.